Annual Mixed Layer Carbon Budget for the West Antarctic Peninsula Continental Shelf: Insights From Year-Round Mooring Measurements

Bo Yang[1,2,3] , **Elizabeth H. Shadwick**[4] , **Cristina Schultz**[1] , **and Scott C. Doney**[1]

[1]Department of Environmental Sciences, University of Virginia, Charlottesville, VA, USA, [2]Cooperative Institute for Marine and Atmospheric Studies, Rosenstiel School of Marine and Atmospheric Science, University of Miami, Miami, FL, USA, [3]Atlantic Oceanographic and Meteorological Laboratory (AOML), NOAA, Miami, FL, USA, [4]CSIRO Oceans and Atmosphere, Hobart, TAS, Australia

Abstract For the first time the annual carbon budget on the West Antarctic Peninsula shelf was studied with continuously measured CO_2 system parameters (pH and $p CO_2$) from a subsurface mooring. The temporal evolution of the mixed layer dissolved inorganic carbon (DIC) is investigated via a mass balance. The annual mixed layer DIC inventory change was 1.1 ± 0.4 mol m^{-2} yr^{-1}, which was mainly regulated by biological drawdown (-2.8 ± 2.4 mol m^{-2} yr^{-1}), diapycnal eddy diffusion (2.6 ± 1.3 mol m^{-2} yr^{-1}), entrainment/detrainment (0.9 ± 0.4 mol m^{-2} yr^{-1}), and air-water gas exchange (0.4 ± 2.1 mol m^{-2} yr^{-1}). Significant carbon drawdown was observed in the spring and summer, which was replenished by the physical processes mentioned above. These observations suggest this area is an annual atmosphere CO_2 sink with a mixed layer net community production of 2.8 ± 2.4 mol m^{-2} yr^{-1}. These results highlight the significant seasonality in the DIC mass balance and the necessity of year-round continuous observations for robust assessments of biogeochemical cycling in this region.

Plain Language Summary With continuously measured CO_2 system parameters (pH and $p CO_2$) from submerged sensors on an oceanographic mooring, for the first time we captured the seasonal and annual changes of surface dissolved inorganic carbon (DIC) on the West Antarctic Peninsula shelf. The annual DIC inventory change was mainly controlled by biological consumption of DIC (e.g., DIC consumption from photosynthesis). Physical processes like diffusion, upwelling/downwelling, and air-water CO_2 exchange also played important roles. Significant biological consumption of DIC was observed in the spring and summer, which was replenished by the physical processes mentioned above. These observations suggest that over a complete seasonal cycle, this area absorbs CO_2 from the atmosphere and produces significant amount of organic carbon through photosynthesis. These results highlight the significant seasonal variations in the DIC mass balance and the necessity of year-round continuous observations for robust assessments of biogeochemical cycling in this region.

1. Introduction

The Western Antarctic Peninsula (WAP, Figure 1) is a highly productive ocean coastal/shelf region with an estimated annual primary production of over 1.0 Tg C yr^{-1} (Moreau et al., 2015), which supports ample phytoplankton carbon stocks at the base of the polar marine ecosystem (Ducklow et al., 2013). The WAP region is also generally considered as a strong seasonal sink for atmospheric CO_2 (Carrillo et al., 2004; Legge et al., 2017), although some studies (e.g., Roobaert et al., 2019) showed that the northern tip of WAP is a net annual CO_2 source to the atmosphere. The WAP marine ecosystem is largely shaped by the unique physical conditions of the polar, seasonally ice-covered coastal region (Ducklow et al., 2013). The Antarctic Circumpolar Current (ACC) flows eastward along the continental slope of the WAP region, transporting a large volume of warm water just below the surface layer (known as Upper Circumpolar Deep Water, UCDW) (Martinson & McKee, 2012; Martinson et al., 2008). The onshore flow of this warm water mass, primarily through subsea canyons and mesoscale eddies, supplies heat, nutrients and dissolved inorganic carbon (DIC) to the WAP continental shelf with important ecological and biogeochemical impacts (Ducklow et al., 2013; Hauri et al., 2015). Freshwater input from sea-ice melting and glacial runoff also have strong
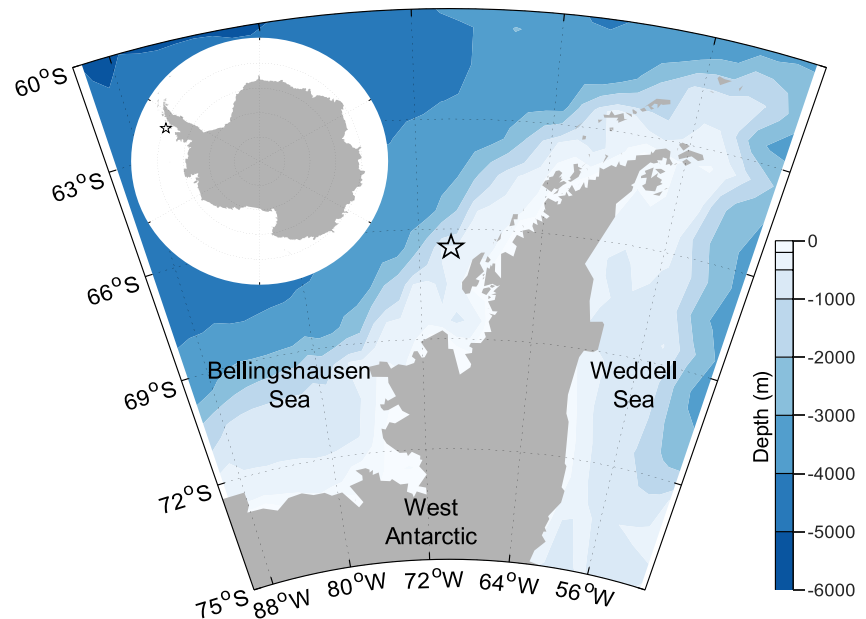
Figure 1. Map of the West Antarctic Peninsula (WAP) with the mooring location (66.5°S, 69.948°W) indicated by the star and water depth indicated with the color bar.

influence on the system. For example, stratified conditions created by freshwater input and presumable iron source from glacial runoff can lead to enhanced phytoplankton carbon fixation (Schofield et al., 2018).

Over the past several decades, the WAP marine ecosystem has undergone substantial environmental changes, such as atmospheric and oceanic warming (Martinson et al., 2008; Meredith & King, 2005; Schofield et al., 2010; Turner et al., 2014), sea-ice and glacier retreat (Cook et al., 2005; Stammerjohn et al., 2012; Stammerjohn et al., 2008a), and large-scale climate variability associated with the Southern Annular Mode (SAM) and the El Niño/Southern Oscillation (Marshall, 2003; Stammerjohn et al., 2008b). These physical changes impact seasonal nutrient drawdown (Kim et al., 2016), phytoplankton primary production (Kim et al., 2018; Montes-Hugo et al., 2009; Moreau et al., 2015), bacterial production (Kim & Ducklow, 2016), secondary production (Ducklow et al., 2013), and ultimately biological carbon production and global carbon cycling.

The general seasonal cycle of the mixed layer carbon dynamics in the WAP shelf can be described as follows. In the winter, the respiration of marine organisms and the entrainment of DIC-rich UCDW due to the deepened mixed layer leads to the increase of DIC in the mixed layer (Carrillo et al., 2004; Hauri et al., 2015; Legge et al., 2017; Tortell et al., 2014; Wang et al., 2010). At the same time, the winter entrainment also supplies macro- and micro-nutrients to the upper ocean (Brown et al., 2019; Joy-Warren et al., 2019). From spring to summer, the shoaling mixed layer, increased light availability, and nutrient availability provide favorable conditions for phytoplankton growth, which lead to significant nutrient/DIC drawdown and organic carbon production (Brown et al., 2019; Carrillo et al., 2004; Hauri et al., 2015; Joy-Warren et al., 2019; Legge et al., 2017; Tortell et al., 2014; Wang et al., 2010). The reported peak chlorophyll (0–50 m, depth-integrated) was around 118 mg m^{-2} (Kim et al., 2016). After summer, the DIC increases in the deepening mixed layer, as the phytoplankton growth decreases, community respiration continues, and the deep mixing entrains high-DIC deep water (Legge et al., 2017; Wang et al., 2010).

The summer-time carbon system dynamics in WAP shelf has been studied extensively, especially through the Palmer Long-Term Ecological Research (PAL-LTER) program (Ducklow et al., 2013). Historical records (largely restricted to the summer season) of seawater DIC, total alkalinity (TA), and nutrients in this area are available since 1993 (Hauri et al., 2015). The summer carbon production has been studied using data from research cruises and PAL-LTER station, including net community production (NCP) derived from O$_2$/Ar of the surface water (e.g., Huang et al., 2012; Tortell et al., 2014), net primary production (NPP) estimated

from ^{14}C deck incubation (e.g., Ducklow et al., 2018), new production from ^{15}N deck incubation (e.g., Stukel et al., 2015), gross primary production (GPP) calculated from surface water triple oxygen isotope composition (e.g., Huang et al., 2012), and export production (EP) estimated from sediment traps or ^{238}U:^{234}Th disequilibrium (e.g., Ducklow et al., 2018). These studies show that the summer-time high new production is not balanced by the export production, which is most likely due to other processes (e.g., vertical mixing, active transport through food web) (Ducklow et al., 2018). However, we lack data from other seasons (especially winter) and therefore a broader understanding of the seasonality on the WAP shelf. While there were some data from discrete sampling or biogeochemical Argo profiling floats, they are generally restricted to the coastal zone (Legge et al., 2015; Legge, et al., 2017) or seasonal sea-ice zone further offshore (e.g., Gray et al., 2018; Williams et al., 2018). In this work, for the first time, we used the data from a subsurface mooring to investigate the annual carbon budget on the WAP shelf, in the context of temporal evolution of the mixed layer dissolved inorganic carbon (DIC) mass balance. The seasonal evolution of the major terms that contribute to the mixed layer DIC budget was identified and diagnosed (with uncertainty analysis), and the biological carbon production was estimated in terms of NCP.

2. Methods

2.1. Data Acquisition

The CO_2 system instrumentation was deployed at the depth of ∼20 m at station 300.100 (66.5°S, 69.9°W, Figure 1) of the Palmer LTER grid in approximately 480 m water depth as an addition to an existing physical oceanographic mooring (Martinson & McKee, 2012) (details of the mooring setup are included in the supporting information). The CO_2 system instrumentation consisted of a pH sensor package (SeapHOx, measuring pH in total scale, temperature, and salinity) and a pCO_2 sensor (ProOceanus), with a sample frequency of 3-h (binned to 1-day resolution in the model described in Section 2.3). Data used in this work came from two deployments in 2017 (December 2016 to April 2017) and 2018 (January 2018 to January 2019), representing the CO_2 system dynamics in the surface mixed layer. While pH observations were available for both deployments, the seawater pCO_2 data was only available for part of the 2018 deployment. Therefore, the CO_2 system calculation was based on pH and salinity-derived total alkalinity (see Section 2.2 for details). The measured pH values were calibrated against the pH values calculated from underway pCO_2 data collected on board the ship in the vicinity of the mooring location and salinity-derived TA (Shadwick et al., 2021). Salinity data for the 2018 deployment was incomplete (stopped in May 2018), and therefore was filled with results from a 3-D regional ocean model (Saenz & Arrigo, 2014; Schultz, 2019; Schultz et al., 2020).

Because salinity data was only available at one depth, the mixed layer depth (MLD) was determined using the mooring temperature profile data. Additional temperature and pressure data obtained from the physical oceanographic mooring were used to determine the MLD. Overall, there were 11 depth levels of temperature data available from 12 to 110 m (12, 17, 25, 34, 42, 50, 58, 66, 74, 90, and 110 m, Figure S1), with a sample frequency of 15-min. The raw data was interpolated (linear interpolation) vertically with a 1-m depth resolution (values from sea surface to 12 m were considered uniform), binned with a 1-day window, and then the daily MLD was calculated using a temperature criterion (0.2°C difference from 10 m).

Atmospheric CO_2 data (in terms of dry-air mole fraction of CO_2, $xCO_{2, air}$, ppm) was obtained from the nearby Palmer Station (64.92°S, 64°W, https://www.esrl.noaa.gov/gmd/dv/site/index.php?stacode=PSA), and then converted to partial pressure ($pCO_{2, air}$, µatm). Wind speed at 10 m (U_{10}) was calculated using 10 m U-wind and V-wind data from the NCEP/NCAR reanalysis (https://psl.noaa.gov/data/gridded/data.ncep.reanalysis.surfaceflux.html). Sea-ice concentration (SIC, %) came from the NOAA OI SST V2 High Resolution Data set (https://www.esrl.noaa.gov/psd/data/gridded/data.noaa.oisst.v2.highres.html).

2.2. CO_2 System Calculation

Total alkalinity (TA, µmol kg^{-1}) was calculated from salinity (S) using a TA-S relationship from 20-year-long Palmer LTER seawater inorganic carbon time series (Figure A2 of Hauri et al. [2015]): TA = 57.01 ($\pm$0.88) × S + 373.86 ($\pm$35.26) µmol kg^{-1}. The seawater DIC and pCO_2 ($pCO_{2, water}$) were then calculated with the pH-TA pair using the CO2SYS MATLAB* version (Van Heuven et al., 2011). The calculation

was performed on the total pH scale with the carbonate dissociation constants ($K_1^{'}$ and $K_2^{'}$) from Lueker et al. (2000) following Deppeler et al. (2018), HSO_4^{-} dissociation constant from Dickson et al. (1990), and the boron to chlorinity ratio from Lee et al. (2010). DIC was normalized to the mean salinity of each deployment, to eliminate the influence from evaporation, dilution, and sea-ice formation/melting.

2.3. Mixed Layer Carbon Mass Balance Model

The mixed layer carbon mass balance model used for DIC budget calculation was similar to the DIC models used in Fassbender et al. (2016) and Yang et al. (2018). The DIC mass balance is summarized with Equation 1. The left-hand side of Equation 1 is the time rate of change of DIC inventory in the mixed layer, integrated from the surface to the mixed layer depth (MLD). The right-hand side of Equation 1 reflects DIC sources and sinks within the mixed layer and DIC fluxes across the upper and lower boundaries of the mixed layer, with all terms defined as positive when the process adds DIC to the mixed layer. Terms include DIC fluxes from entrainment/detrainment (F_{Ent}), biological net carbon production (F_{Bio}), air-water gas exchange (F_{A-W}), diapycnal eddy diffusion (F_{kz}), and vertical advection (F_w). The time step of this mass balance model Δt is taken as 1-day to reflect mooring instrument sampling frequency and temporal resolution of forcing data sets, and therefore all the input data for the model were binned to 1-day resolution. Although the information of diel cycle was lost with the daily mean, it would not affect the cumulative carbon flux and our analysis on the annual carbon mass balance over a complete seasonal cycle. A 30-day moving average (time-centered) was then applied to the data set (except for Ekman pumping rate) to filter out short-term fluctuations, so that we could focus on the seasonal evolution of the carbon system dynamics. The 30-day window corresponds roughly to the residence time of CO_2 gas in the upper ocean without accounting for the delays due to buffering with the larger DIC pool (Emerson & Hedges, 2008). It should be noted that the DIC was converted from the standard unit ($\mu mol\ kg^{-1}$) to $mmol\ m^{-3}$ using the density calculated from mixed layer salinity and temperature, so that the final unit of Equation 1 is $mmol\ m^{-2}\ d^{-1}$.

$$\frac{d\text{MLD}\cdot\text{DIC}}{dt} = F_{Ent} + F_{Bio} + F_{A-W} + F_{kz} + F_w \ \text{mmol m}^{-2}\text{d}^{-1} \tag{1}$$

The DIC flux from entrainment and detrainment was calculated using Equations 2 or 3, depending on the sign of the derivative of MLD with respect to time. When the mixed layer is deepening ($d\text{MLD}/dt > 0$), the water below is entrained into the new (deepened) mixed layer, and therefore F_{Ent} is positive (Equation 2). In contrast, when the mixed layer is shoaling, water is detrained from the original mixed layer and F_{Ent} is negative (Equation 3).

a) MLD deepening ($d\text{MLD}/dt > 0$)

$$F_{Ent} = \frac{d\text{MLD}}{dt}\cdot\text{DIC}_{below} \ \text{mmol m}^{-2}\text{d}^{-1} \tag{2}$$

b) MLD shoaling ($d\text{MLD}/dt < 0$)

$$F_{Ent} = \frac{d\text{MLD}}{dt}\cdot\text{DIC}_{MLD} \ \text{mmol m}^{-2}\text{d}^{-1} \tag{3}$$

The DIC of water entrained from below the mixed layer (DIC_{below}) was calculated with mixed layer DIC (DIC_{MLD}), the change of MLD over a model time step Δt ($\Delta\text{MLD} = \text{MLD}_{deepened} - \text{MLD}_{original}$), and the DIC gradient below the base of the mixed layer ($d\text{DIC}/dz$, $mmol\ m^{-4}$). The details are presented in the supporting information.

The salinity-normalized DIC gradient was obtained from a separate, 3-D modeled seasonal climatology (Schultz, 2019; Schultz et al., 2020). For each mixed layer DIC model time step, dDIC/dz below the corresponding MLD was calculated using the climatological DIC profile from the 3-D model outputs.

Flux from air-water gas exchange (F_{A-W}) was calculated using the wind speed dependent parameterization from Wanninkhof (2014), where k and K_0 are gas transfer velocity and CO_2 solubility, respectively, and 10-m

wind speed is computed from the NCEP data. When $pCO_{2,\,air}$ is greater than $pCO_{2,\,water}$ the CO_2 flux goes from the atmosphere to the ocean (adding CO_2 into the ocean mixed layer), and therefore $F_{A\text{-}W}$ is positive for the ocean.

$$F_{A\text{-}W} = k \cdot K_0 \cdot \left(pCO_{2,air} - pCO_{2,water} \right) \text{mmol m}^{-2}\text{d}^{-1} \tag{4}$$

Because sea-ice fields formed seasonally in this region, a sea-ice correction factor was applied to $F_{A\text{-}W}$ following the methods from Takahashi et al. (2009) and Evans et al. (2015). Briefly, the area is considered to be open water (100% air-sea flux) when sea-ice concentration (SIC) is less than 10%; for SIC between 10% and 90%, the air-sea flux is proportional to open water area (1-SIC); the air-sea flux is considered to be 10% of open water condition when SIC was greater than 90%.

Flux from diapycnal eddy diffusion (F_{kz}) at the base of the mixed layer was calculated as the DIC gradient (dDIC/dz, mmol m^{-4}) multiplied by the diapycnal eddy diffusion (k_z, m^2 s^{-1}). A k_z value of 8.5×10^{-5} m^2 s^{-1} was used in this study, as determined by a previous study of the same region (Martinson et al., 2008).

$$F_{kz} = k_z \cdot \frac{d\text{DIC}}{dz} \text{mmol m}^{-2}\text{d}^{-1} \tag{5}$$

In this model, DIC in the mixed layer was considered to be horizontally homogeneous, and therefore only vertical advection was considered. During periods of downwelling, because water in the mixed layer is replenished from the side and the mixed layer is horizontally homogeneous, the incoming and outgoing fluxes cancel each other out, and therefore the net flux due to downwelling is zero ($F_w = 0$). During periods of upwelling, water upwells from below the mixed layer, and the excess water in the mixed layer is pushed to the side (lateral surface divergence). The net DIC flux due to upwelling was calculated using Equation 6, where V_{Ekman} (m d^{-1}) is the Ekman pumping rate, DIC_{advect} (mmol m^{-3}) is the DIC concentration of the advected water, and DIC_{MLD} (mmol m^{-3}) is the DIC concentration in the mixed layer. F_w was also corrected for sea-ice presence using the same correction method used for $F_{A\text{-}W}$ (described above).

$$V_{Ekman} > 0 \left(\text{Upwelling} \right): F_w = F_{w,in} - F_{w,out} = V_{Ekman} \cdot \left(\text{DIC}_{advect} - \text{DIC}_{MLD} \right) \text{mmol m}^{-2}\text{d}^{-1} \tag{6}$$

DIC_{advect} was calculated with the mixed layer DIC concentration (DIC_{MLD}) and the DIC gradient from the 3-D model in a similar fashion to DIC_{below} used in the entrainment flux calculation (see the supporting information for details). The Ekman pumping rate (V_{Ekman}, m d^{-1}) was calculated using the curl of the wind stress field from satellite observations (http://apdrc.soest.hawaii.edu/datadoc/ascat.php).

The time rate of change of mixed layer DIC, term in Equation 1, dMLD·DIC/dt, is calculated diagnostically from the 30-day time filtered mooring physical and chemical data on the model time steps. The biological net carbon production (F_{Bio}) is then computed as the difference between dMLD·DIC/dt and the sum of the other right-hand side terms ($F_{Ent} + F_{A\text{-}W} + F_{kz} + F_w$).

2.4. Uncertainty Analysis

A Monte Carlo approach was used for an uncertainty analysis of the mixed layer DIC mass balance. For "model coefficients" like kz, k, and dDIC/dz, a single random noise value within a specified range was added, and used for all time steps throughout each independent Monte Carlo iteration. On the other hand, for "input data" like pH and V_{Ekman}, the uncertainties (within a specified range) were randomly chosen for each time step within an iteration. Theoretically, MLD should be considered as "input data." However, adding random noise to MLD for each time step could potentially change the sign of dMLD/dt, and thus created artifacts in the budget calculation. Therefore, in this case MLD was treated as a "model coefficient," and a single random noise value was used for all time steps throughout each independent Monte Carlo iteration. The modeled DIC budget was recomputed for 2,000 iterations, and the standard deviation (σ) of the 2,000 resultant values for each term was used as the estimate for the uncertainties. For each input parameter, the range of normally distributed uncertainties (1-sigma or standard deviation) were specified as in Table 1. For pH and salinity, manufacturer stated ranges of instrument errors were used as the uncertainties. Uncertainties of MLD, k_z, and k were assigned to be ±2.0 m (Fassbender et al., 2016), ±50% (Yang et al., 2017),

Table 1
The Assigned Uncertainties (1σ) for Input Parameters

Input parameter	pH	Salinity	MLD	k_z	k for F_{A-W}	dDIC/dz	V_{Ekman}
Uncertainty	±0.01	±0.01	± 2.0 m	±50%	±20%	±10%	±30%

and ±20% (Wanninkhof, 2014), respectively. Uncertainty of salinity-TA proxy is from Hauri et al. (2015). Uncertainties for mixed layer pCO$_2$ and DIC were computed using the CO2SYS program with the Monte Carlo perturbed pH and TA.

3. Results and Discussion

3.1. Observed CO$_2$-System Variables

The annual cycles of pH, seawater and air pCO$_2$, salinity, and temperature are presented in Figure 2, with data from two deployments: 2017 data in gray and 2018 data in blue. The annual cycle from the 2018
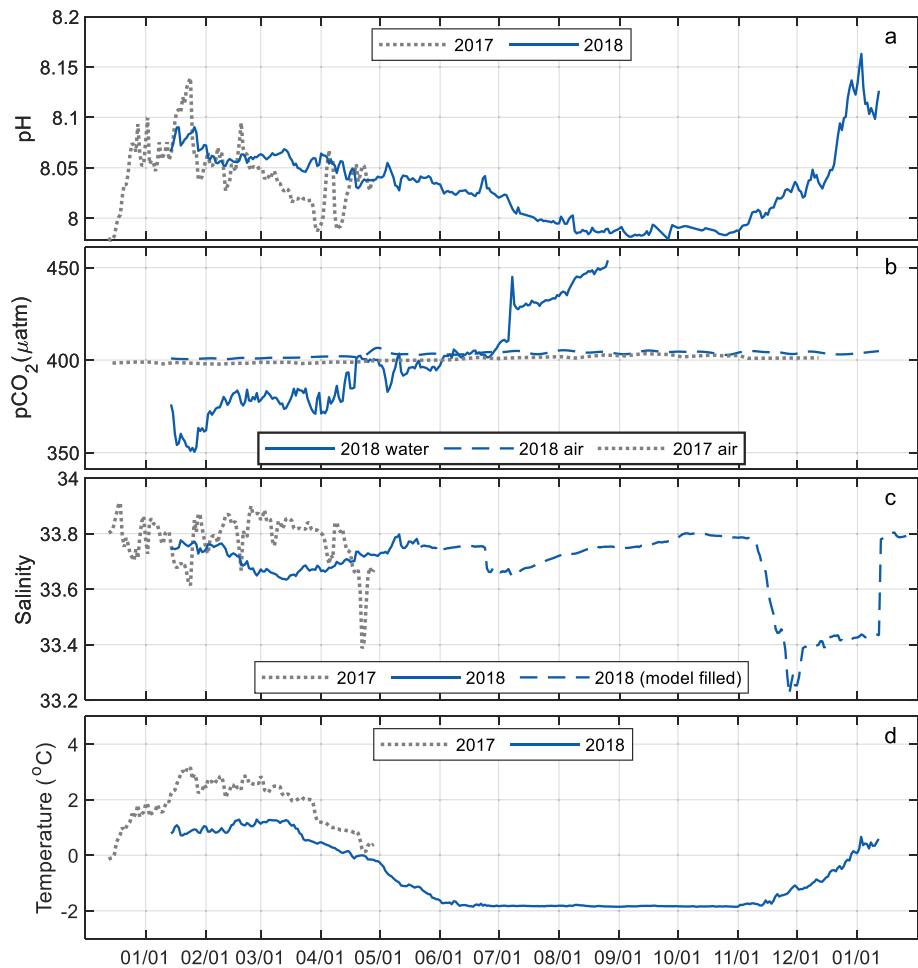

Figure 2. Annual cycles of pH, pCO$_2$ (μatm), salinity, and temperature measured by the WAP mooring. Panel (a): pH from the 2017 and 2018 deployments presented with gray dotted line and blue line, respectively. Panel (b): The seawater pCO$_2$ data was only available for the 2018 deployment (blue solid line), a comparison between measured and calculated seawater pCO$_2$ is presented in the supporting information. The air pCO$_2$ data for 2017 (gray dotted line) and 2018 (blue dash line) was from the US Palmer Station on the Antarctic Peninsula (https://www.esrl.noaa.gov/gmd/dv/site/index. php?stacode=PSA). Panel (c): Salinity data for the 2018 deployment was incomplete, and therefore was filled with model output from Schultz et al. (2020). Panel (d): Temperature from the 2017 and 2018 deployments presented with gray dotted line and blue line, respectively.

deployment was almost complete, with a full-year of pH, 8 months of seawater pCO_2, and 5 months of salinity data (the rest was filled with model output). Therefore, from this point forward our analysis mainly focuses on the 2018 full-year deployment, and the data from the shorter 2016/17 deployment (~5.5 months, from December to May) is used for comparison and to give an indication of inter-annual variability. Note that the mooring deployment and recovery date occurred in the middle of the Austral late-spring and early summer growth season, the timing fixed in part by the Palmer LTER program ship logistics schedule.

Elevated pH (around 8.08) occurred in the 2018–2019 time series right after deployment in January, the height of the summer phytoplankton growth season (Smith et al., 1998), gradually decreased to the lowest value (below 8.0) in August, and remained low through October. pH started increasing again in November and reached a second, even higher pH peak around 8.15 in January, 2019. The overall magnitude and decreasing trends of pH from December to May were similar for both 2017 and 2018 deployments.

The atmospheric pCO_2 data from Palmer station were relatively stable year-round (around 400 μatm), with the 2018 values slightly higher than 2017 as expected due to long-term atmospheric CO_2 growth of roughly 2 ppm/yr (Figure 2b). Seawater pCO_2 from 2018 deployment increased from a minimum of about 350 μatm in January to a maximum of about 450 μatm in August, and seawater pCO_2 mirrored the pH annual cycle. The observed seasonal cycle and maximum winter seawater pCO_2 are close to the results from Ryder Bay of WAP (coastal site), but Ryder bay has a much lower seawater pCO_2 minimum of ~150 μatm (Legge et al., 2017). The annual salinity range from the mooring data was relatively small (between 33.2 and 33.9), with a significant salinity decline (0.4–0.6) from November to January from sea-ice melt and glacial discharge indicated in the ocean 3-D model simulations (Figure 2c). The annual temperature range was about 3°C, with winter temperature close to the freezing point of seawater and summer temperate above zero degree from January to April (Figure 2d).

3.2. Computed Variables

The year-round mixed layer DIC values, computed from the mooring pH observations and alkalinity-salinity relationship, varied between 2,150 and 2,205 μmol kg^{-1} (Figure 3c). The calculated summer DIC values were low in January, 2018 (~2,160 μmol kg^{-1}) and then gradually increased through July. From fall to winter (August to November), the DIC values were steady and high (over 2,200 μmol kg^{-1}), before then dropping rapidly again to an even lower minimum of ~2,150 μmol kg^{-1} in January, 2019. The observed seasonal cycle of mixed layer DIC was similar to previous observations in nearby area (Legge et al., 2015; Legge et al., 2017; Williams et al., 2018). The computed pCO_2 and aragonite saturation state (pCO_2 ranging from 320 to 460 μatm, Ω_{Ar} ranging from 1.2 to 1.6, see the supporting information for details) were also close to the results from the nearby offshore seasonal sea-ice zone (Williams et al., 2018).

The annual evolution of mixed layer depth (MLD) for the 2018 deployment, shown in Figure 3d, exhibits shallow summer MLD in January to February (30–40 m), deepest MLD from August to November (80–90 m), and then a rapid shoaling back to about 40 m in December followed by shallow MLD of ~30 m again in January, 2019. It should be noted that the rapid shoaling of MLD in November, 2018, preceded the significant DIC decrease in December, 2018, by about a month indicating that the shoaling MLD was not the sole reason for the decreasing DIC (see further discussion below). The December to May MLD from 2017 deployment (Figure 3b) was slightly shallower than the 2018 deployment.

The model simulated vertical DIC gradients (dDIC/dz, Figure 4) across the base of the mixed layer (Schultz 2019; Schultz et al., 2020) were relatively small (between 0.5 and 2 mmol m^{-4}), with higher values in the summer, when MLD was shallow, and lower values in winter. Although the same climatological model outputs were used for both years (deployments), the magnitudes of dDIC/dz for the 2017 and 2018 deployments were different due to the difference in the observed MLD, reflecting variations in the vertical profile of dDIC/dz. For most of the year, the Ekman pumping rate (V_{Ekman}) was between −0.5 to +1.5 m d^{-1} with no clear seasonal cycle (Figure 5a). The gap of V_{Ekman} from July to December was due to the unavailability of satellite wind data. However, most of the surface ocean was covered by sea-ice for this period of time (Figure 5b), and the wind-driven upwelling/downwelling (as well as air-sea gas exchange) was negligible. Therefore, the missing V_{Ekman} in the winter did not affect the mass balance calculation.
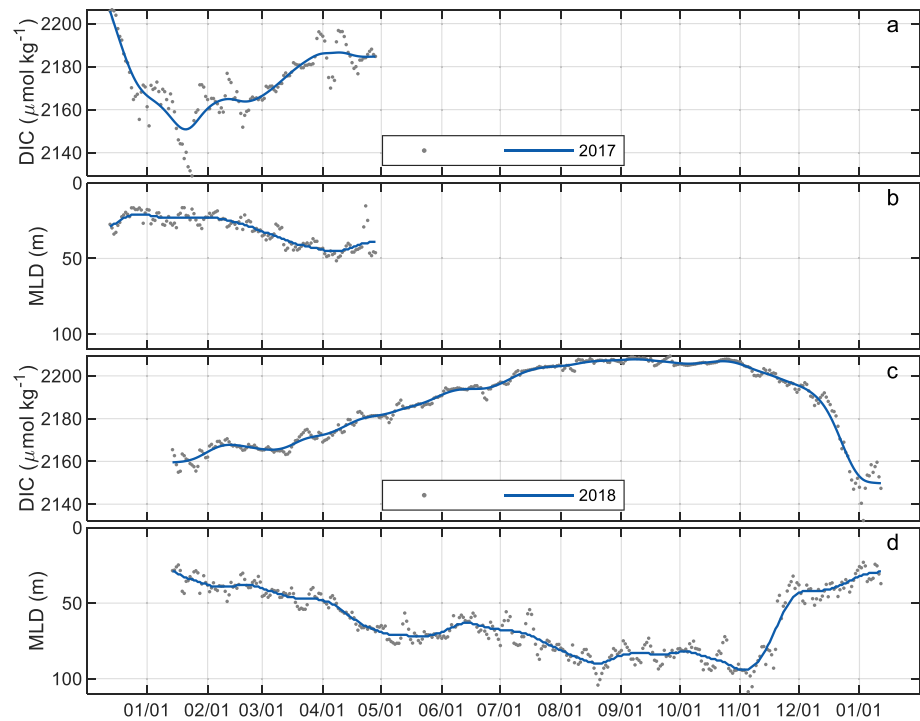
Figure 3. Annual cycles of salinity-normalized dissolved inorganic carbon (DIC, μmol kg⁻¹) and mixed layer depth (MLD, m) for the 2017 (panels a and b) and 2018 (panels c and d) deployments. The gray dots and blue lines indicate the original data and the smoothed (30-day running mean) result, respectively. The DIC values are shown in standard unit (μmol kg⁻¹) in these figures but are converted to mmol m⁻³ using seawater density for use in the model described in Equation 1.

3.3. Mixed Layer Carbon Mass Balance

As shown in Figure 6, the mixed layer integrated DIC inventory change (dMLD·DIC/dt, blue solid lines in panels a and c) was large, on the order of 10^3 mmol m⁻² d⁻¹. As a rough scaling, an inventory change of $+10^3$ mmol m⁻² d⁻¹ would result from a 0.5 md⁻¹ MLD entrainment rate and the background DIC concentration of ~2,100 mmol m⁻³. However, to first order dMLD·DIC/dt also was approximately equal to F_{Ent}, with the trends closely matching for each of the individual deployment periods (as shown in panels b and d, the difference between dMLD·DIC/dt and F_{Ent} is on the order of −80 to 30 mmol m⁻² d⁻¹). This finding indicates that the seasonal variations in the mixed layer integrated DIC inventory were mainly controlled by the entrainment or detrainment due to MLD variation (MLD, yellow line, right axis). Recall that F_{Ent} was positive when mixed layer was deepening and negative when mixed layer was shoaling, with the magnitude of F_{Ent} proportional to the rate of change in MLD (Equations 2 and 3).
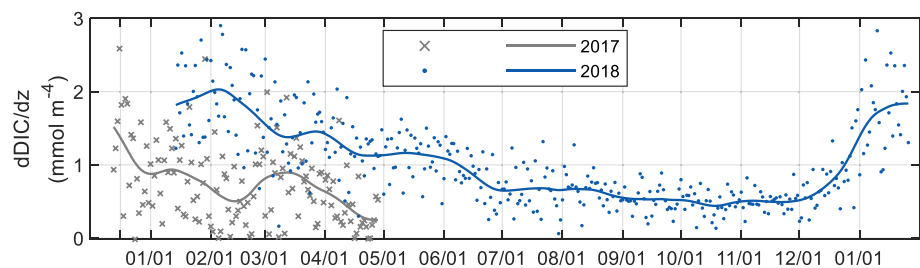

Figure 4. Annual cycles of salinity-normalized DIC gradients (dDIC/dz, mmol m⁻⁴) across the base of the mixed layer. The gradient was a seasonal climatology calculated from a 1991–2014 model result (Schultz, 2019; Schultz et al., 2020). The gray dots and blue crosses indicate the original data, and the smoothed (30-day running mean) are presented in gray and blue lines.
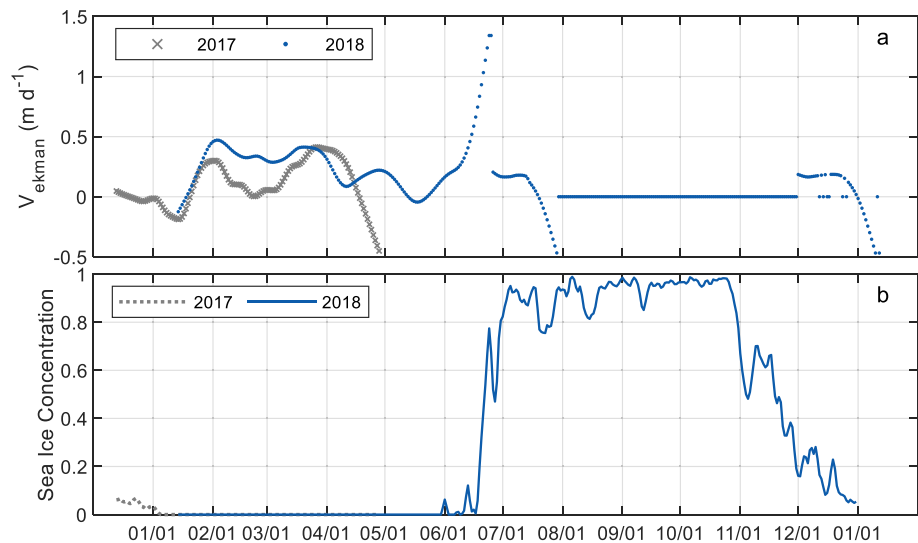
Figure 5. Annual cycle of (a): Ekman pumping rate (V_{Ekman}, m d^{-1}, corrected for sea-ice coverage), and (b) sea-ice concentration (SIC, fraction from 0 to 1). V_{Ekman} was calculated from Advanced Scatterometer (ASCAT) Surface Wind Fields data (http://apdrc.soest.hawaii.edu/datadoc/ascat.php), and SIC was from NOAA Earth System Research Lab (https://www.esrl.noaa.gov/psd/data/gridded/data.noaa.oisst.v2.highres.html). It should be noted that the DIC flux from Ekman pumping (F_w) was also corrected for sea-ice presence using the same correction method used for F_{A-W}.

Although the seasonal variation in dMLD·DIC/dt was mainly controlled by F_{Ent}, the net (cumulative) flux of F_{Ent} was not as significant for the annual DIC budget because the MLD and DIC returned to roughly similar summer values after a full seasonal cycle from January 2018 to January 2019 (Figure 3). As shown in Table 2, after a full annual cycle the mixed layer integrated DIC inventory for the 2018 deployment increased by only $+1.1 \pm 0.4$ mol m^{-2}. For comparison, the annual mean entrainment term F_{Ent} was similar at $+0.9 \pm 0.4$ mol m^{-2}, and the quantity (dMLD·DIC/$dt - F_{Ent}$) was approximately zero. Furthermore, because the uncertainties of both F_{Ent} and dMLD·DIC/dt are dependent to MLD and DIC, they cancel each other out and the uncertainty in the residual flux (dMLD·DIC/$dt - F_{Ent}$) is relatively small (see the last paragraph of this section and Figure 9a).

Other physical and biological fluxes, therefore, also contributed significantly to the net annual mixed layer DIC budget. The seasonality and relative magnitudes of F_{Bio}, F_{A-W}, F_w, and F_{kz} are shown in Figure 7, and the mixed layer DIC mass balance after a full seasonal cycle (in terms of annual flux for each term) is presented in Table 2. The annual inventory balance was mainly controlled by fluxes from biological processes (F_{Bio}, -2.8 ± 2.4 mol m^{-2} yr^{-1}), diapycnal eddy diffusion (F_{kz}, 2.6 $\pm$ 1.3 mol m^{-2} yr^{-1}), entrainment/detrainment (F_{Ent}, 0.9 $\pm$ 0.4 mol m^{-2} yr^{-1}), and air-water gas exchange (F_{A-W}, 0.4 $\pm$ 2.1 mol m^{-2} yr^{-1}).

Flux from biological processes (F_{Bio}, red dash dotted line in Figure 7) was one of the most important terms in the annual mixed layer carbon budget (-2.8 mol m^{-2} yr^{-1}, Table 2). F_{Bio} was mostly negative in the spring and summer phytoplankton growth season (November to March), indicating net biological DIC uptake, and positive from May to September, indicating net respiration and remineralization releasing DIC into the mixed layer. The most significant DIC drawdown (due to biological process) occurred in December (for both years). The polar plankton community in the WAP region has relative low contributions from calcifying plankton (Garibotti et al., 2003; Montes-Hugo et al., 2009) and a weaker regional biological alkalinity signal relative to DIC (Hauri et al., 2015). Therefore, the majority of the seasonal F_{Bio} cycle likely was due to biological production and consumption of organic carbon (which took up or released DIC), with a considerably smaller portion due to the formation/dissolution of calcium carbonate. Therefore, the net biological DIC flux (F_{Bio}) can be used as an upper limit estimate of the mixed layer net community production (NCP $= -F_{Bio}$); note that the model does not capture any seasonal NCP signals in the seasonal thermocline below the mixed layer.

Table 2
Net Annual Mixed Layer DIC Mass Balance With Model Fluxes From the 2018 Deployment Year Averaged Over the Full Annual Cycle (unit: mol m^{-2} yr^{-1}, Positive Value Indicates DIC Added to the Mixed Layer)

Annual flux (mol m^{-2} yr^{-1})						
$\dfrac{d\text{MLD·DIC}}{dt} = F_{\text{Ent}} + F_{\text{Bio}} + F_{\text{A-W}} + F_{\text{kz}} + F_{\text{w}}$						
$\dfrac{d\text{MLD·DIC}}{dt}$	F_{Ent}	F_{Bio}	$F_{\text{A-W}}$	F_{kz}	F_{w}	aNCP $\approx -F_{\text{Bio}}$
1.1 ± 0.4	0.9 ± 0.4	-2.8 ± 2.4	0.4 ± 2.1	2.6 ± 1.3	0.03 ± 0.02	2.8 ± 2.4

Note. The annual Net Community Production (aNCP) for the system is approximated as the negative of the mixed layer model estimated biological net carbon production term, F_{Bio}, which is computed as the time rate of change in the mixed layer DIC inventory ($d\text{MLD·DIC}/dt$) minus the sum of the remaining right-hand side terms from Equation 1 ($F_{\text{Ent}} + F_{\text{A-W}} + F_{\text{kz}} + F_{\text{w}}$). It should be noted that the DIC values had been normalized with salinity.

The seasonal phenology and magnitude of F_{Bio} from the CO_2 mooring data and mixed layer DIC mass balance model were broadly similar to NCP estimates from regional measures of new production, NCP, and export production (e.g., Ducklow et al., 2018; Kim et al., 2016). In our case, the annual cumulative F_{Bio} was -2.8 mol m^{-2} yr^{-1}, indicating an upper limit of mixed layer integrated annual NCP (aNCP) of 2.8 mol m^{-2} yr^{-1} (Table 2). This aNCP value was consistent with the upper limit of the historical aNCP estimates from the Weddell Sea region (3.5 mol m^{-2} yr^{-1}, Hoppema et al., 2007) and Palmer Station (2.7 mol m^{-2} yr^{-1}, estimated from annual nitrate drawdown, Kim et al., 2016). Compared with those above-mentioned historical studies based on summer-time sampling, the year-round mooring data used in this study gives us a much better sense of the seasonal variations in NCP. As shown in Figure 8 (note that the starting time is set to September to highlight the growth season), the mixed layer integrated NCP (yellow line) turned positive in September and continued increasing, causing the cumulative NCP (blue dotted line) to increase as well. The peak of NCP occurred in mid-December, while the peak of cumulative NCP was slightly lagged (occurred in late December). The summer NCP value was between 30 and 95 mmol m^{-2} d^{-1} (equivalent to 0.4–2.5 mmol m^{-3} d^{-1}), which was comparable to the summer NCP estimates from previous studies in the WAP Palmer grid (1.3–1.9 mmol m^{-3} d^{-1}, Carrillo et al., 2004; 40–80 mmol m^{-2} d^{-1}, Ducklow et al., 2018; 30–60 mmol m^{-2} d^{-1}, Eveleth et al., 2017) and Ross Sea (0.5–2.5 mmol m^{-3} d^{-1}, Bates et al., 1998; 0.3–1.4 mmol m^{-3} d^{-1}, Sweeney et al., 2000). After the summer peak, NCP decreased rapidly (with cumulative NCP decreasing accordingly but in a lower rate) and had some fluctuations in January, February and March, which was most likely due to strong respiration and decreasing primary production (Joy-Warren et al., 2019). From mid-April to late August NCP stayed negative (indicating net respiration), with cumulative NCP decreasing faster than early fall.

Fluxes from diapycnal eddy diffusion (F_{kz}, green line in Figure 7) were also significant, with an annual flux of 2.6 mol m^{-2} yr^{-1}. F_{kz} was always positive because the DIC below the mixed layer was always higher than that within the mixed layer (positive $d\text{DIC}/dz$, as shown in Figure 4), and therefore replenished the net biological drawdown of DIC in the mixed layer. Higher F_{kz} was observed in the summer, because the summer mixed layer was shallower (Figure 3d) and the vertical DIC gradient at the base of the mixed layer was larger (Figure 4).

The air-water gas exchange flux ($F_{\text{A-W}}$, yellow dash line in Figure 7) was positive from mid-November to June, indicating CO_2 flux from the atmosphere to the ocean. From June to November the surface ocean was mostly covered by the sea-ice (Figure 5b), and therefore $F_{\text{A-W}}$ was relatively small with most valued near zero or slightly negative. The annual $F_{\text{A-W}}$ was positive at 0.4 mol m^{-2} yr^{-1} (Table 2), close to the estimate of ~ 0.7 mol m^{-2} yr^{-1} from Roobaert et al. (2019) (gridded monthly air-sea CO_2 flux derived using seawater $p\text{CO}_2$ from artificial neural network interpolation) for this shelf region, but smaller than the estimates from near-shore coastal zone (Ryder Bay, 0.9–1.4 mol m^{-2} yr^{-1}, based on discrete sampling [Legge et al., 2015]) and the more pelagic seasonal sea-ice zone (~ 1.6 mol m^{-2} yr^{-1}, based on BGC-Argo measurements (Gray et al., 2018)). A complementary analysis focused on air-water CO_2 exchange using the mooring data is presented in Shadwick et al., (2021).
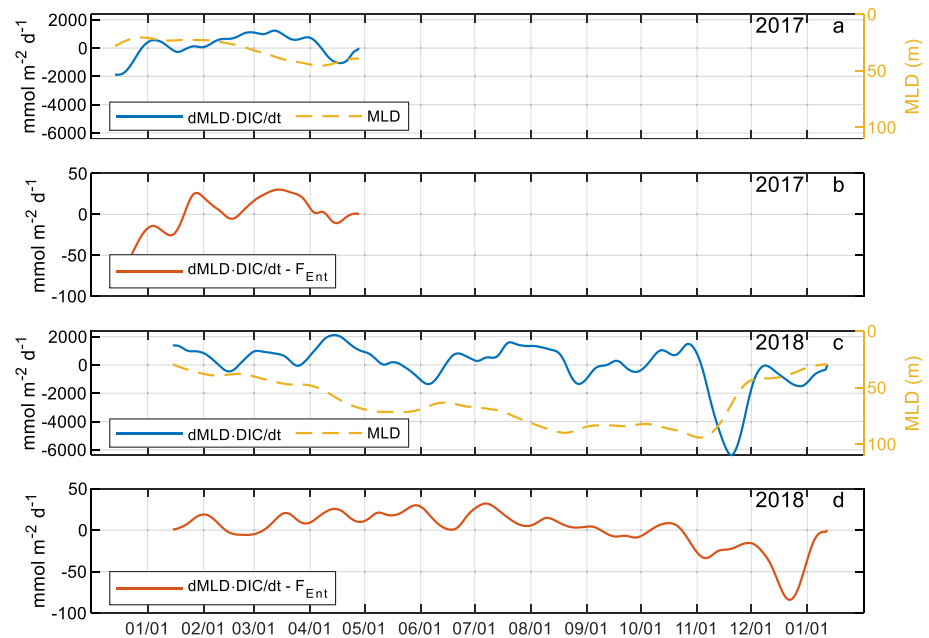
Figure 6. (a and c) Annual cycle of DIC inventory change in the mixed layer (dMLD·DIC/dt, mmol m^{-2} d^{-1}), and mixed layer depth (m). (b and d) Annual cycle of dMLD·DIC/dt − F_{Ent}. Data in panels were from the 2017 and 2018 deployments, respectively. It should be noted that the DIC values had been normalized with salinity.

Flux from wind-driven vertical advection (F_{Ekman}, purple line) was insignificant, due to the relatively low and variable Ekman pumping rate, relatively small DIC gradient across the base of the mixed layer, as well as the sea-ice coverage in the winter. The detailed seasonal evolution of F_{Ekman} is presented in the supporting information (Figure S5).
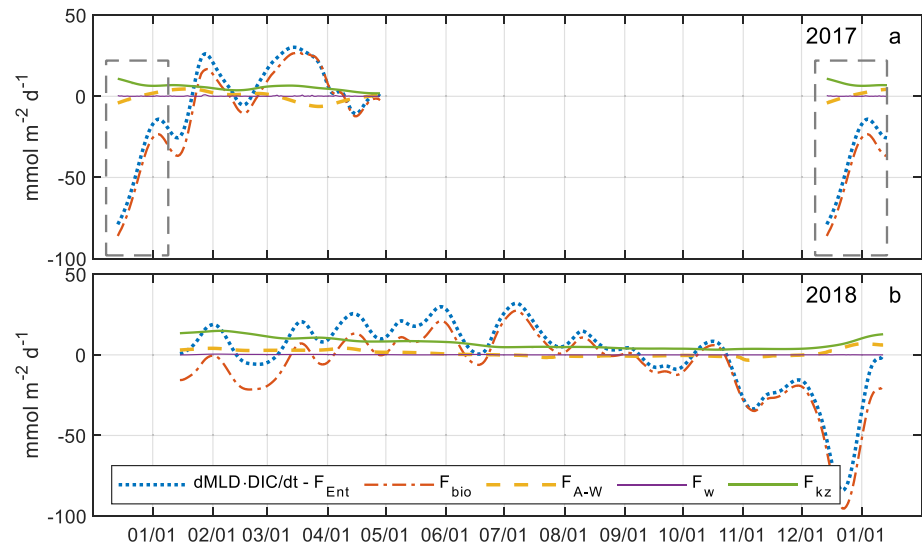

Figure 7. Annual cycles of (salinity-normalized) DIC fluxes (mmol m^{-2} d^{-1}) from biological net carbon production (F_{bio}, red dotted-dash line), air-water gas exchange (F_{A-W}, yellow dash line), vertical advection (F_w, purple line, see supporting information for details), and diapycnal eddy diffusion (F_{kz}, green line). Positive flux indicates DIC increase in the mixed layer, while negative flux indicates DIC drawdown. In panel (a), data from December 2016 to January 2017 (as indicated by the rectangle) was replicated on the right side of the panel, so that it could be compared more easily with the data from the 2018 deployment (panel b).
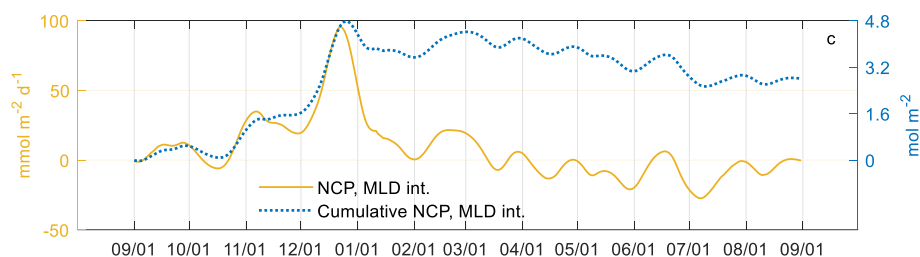
Figure 8. The annual evolution of mixed layer integrated NCP (yellow line) and mixed layer integrated cumulative NCP (blue dotted line). Note that the starting time is set to September (when the sustained period of positive NCP starts) to highlight the growth season in the spring (September to November) and summer (December to February), assuming that the 2018 data is representative of a full, repeating annual cycle.

Although the 2017 deployment did not cover a complete annual cycle, the limited data from December to May (Figure 7a) showed seasonal variations in mixed layer carbon mass balance similar to the 2018 deployment (Figure 7b), with some components having differences in magnitude and timing. For example, F_{Bio} in March was higher in 2017 deployment, and the maximum biological DIC drawdown happened ~1 week earlier in 2017. Such differences suggest potential inter-annual variations in the carbon system dynamics. Furthermore, since F_{Bio} and F_{kz} are two of the most important terms in the DIC mass balance and both processes can be influenced by the rapid regional environmental change (e.g., enhanced nutrient supply from UCDW (Turner et al., 2014); shifting phytoplankton community structure (Ducklow et al., 2013); increased upper ocean stability (Brown et al., 2019)), mooring-based continuous monitoring would be the ideal approach for studying the inter-annual and long-term variations in regional carbon cycle.

The uncertainty estimates of all the fluxes in Equation 1 are presented in Figure 9. Despite the relatively large uncertainty of the DIC calculated with pH and TA from salinity-TA proxy ($\sim\pm33$ μmol kg^{-1}, not shown in Figure 9), the uncertainty in dMLD·DIC/$dt - F_{Ent}$ (Figure 9a) is relatively small (with the largest uncertainty of $\sim$30 mmol m^{-2} d^{-1}) because the uncertainties of both terms (dMLD·DIC/dt and F_{Ent}) are dependent to MLD and DIC and thus cancel out each other. Uncertainties from F_{kz} (Figure 9b) were between 2 and 8 mmol m^{-2} d^{-1}. The uncertainty of F_{A-W} (Figure 9d) was relatively large with the largest uncertainty close to 50 mmol m^{-2} d^{-1}. Because flux from vertical advection was insignificant in the mass balance, uncertainty from F_w (Figure 9c) also contributed the least. Ultimately, uncertainties from all those terms above resulted in the uncertainty in the calculated net biological flux of DIC (F_{Bio}) between 5 and 15 mmol m^{-2} d^{-1} for most of the year. And the uncertainties for the annual flux of each term has been shown in Table 2.

4. Conclusion

The CO$_2$ mooring observations and subsequent modeling yield the first highly temporally resolved annual cycle of the mixed layer carbon system dynamics on the WAP shelf. Overall, our results showed that the seasonal mixed layer carbon budget (mixed layer integrated DIC inventory) was mainly controlled by biological processes, diapycnal eddy diffusion, entrainment/detrainment (due to mixed layer change), and air-water gas exchange. The DIC consumed by the biological processes was replenished by other process (e.g., entrainment/detrainment, air-sea gas exchange, eddy diffusion), which was also suggested by previous a study (Montes-Hugo et al., 2010). Our result supported the idea that the WAP shelf was an important biological carbon sink with overall positive air to water CO$_2$ flux (F_{A-W}) and positive aNCP (Brown et al., 2019). Mooring-based long-term observation has several advantages over other approaches. For example, it can provide high temporal resolution information that cannot be covered with discrete sampling (especially in the winter), and the fixed location makes it possible to study the inter-annual and long-term variations in the carbon system dynamics (Argo floats are only deployed in the deeper offshore area, and the inter-annual variation is difficult to be captured with constantly moving floats). Considering the importance of the WAP shelf (as well as other high-latitude seasonal sea-ice zones under rapid regional environmental change) in the global carbon cycle, it is useful to develop and deploy new autonomous platforms with multi-parameter CO$_2$ sensor packages for continuous measurements of CO$_2$ system parameters covering large temporal,
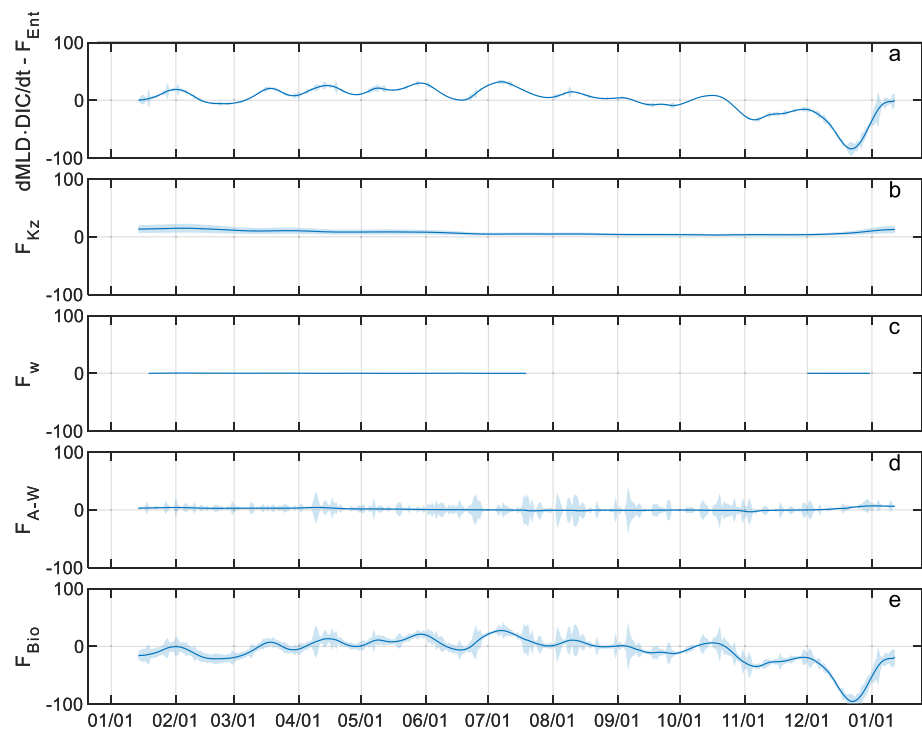
Figure 9. The uncertainty analysis result of all DIC fluxes (mmol m^{-2} d^{-1}) in Equation 1 for the 2018 deployment. We combined the terms of dMLD·DIC/dt and F_{Ent} together in panel (a), so that the scale could be close to other fluxes and easier for comparison. It should be noted that the DIC values had been normalized with salinity.

spatial, and depth scales, which will largely advance our understanding of CO_2 system and carbon cycle in this area.

Data Availability Statement

The mooring data are available at William & Mary's ScholarWorks (https://scholarworks.wm.edu/data/427/, https://doi.org/10.25773/0nxb-wm54).

References

Bates, N. R., Hansell, D. A., Carlson, C. A., & Gordon, L. I. (1998). Distribution of CO_2 species, estimates of net community production, and air-sea CO_2 exchange in the Ross Sea polynya. *Journal of Geophysical Research*, *103*(C2), 2883–2896. https://doi.org/10.1029/97jc02473

Brown, M. S., Munro, D. R., Feehan, C. J., Sweeney, C., Ducklow, H. W., & Schofield, O. M. (2019). Enhanced oceanic CO_2 uptake along the rapidly changing West Antarctic Peninsula. *Nature Climate Change*, *9*, 678–683. https://doi.org/10.1038/s41558-019-0552-3

Carrillo, C. J., Smith, R. C., & Karl, D. M. (2004). Processes regulating oxygen and carbon dioxide in surface waters west of the Antarctic Peninsula. *Marine Chemistry*, *84*(3–4), 161–179. https://doi.org/10.1016/j.marchem.2003.07.004

Cook, A. J., Fox, A. J., Vaughan, D. G., & Ferrigno, J. G. (2005). Retreating glacier fronts on the Antarctic Peninsula over the past half-century. *Science*, *308*(5721), 541–544. https://doi.org/10.1126/science.1104235

Deppeler, S., Petrou, K., Schulz, K. G., Westwood, K., Pearce, I., McKinlay, J., & Davidson, A. (2018). Ocean acidification of a coastal Antarctic marine microbial community reveals a critical threshold for CO_2 tolerance in phytoplankton productivity. *Biogeosciences*, *15*(1), 209–231. https://doi.org/10.5194/bg-15-209-2018

Dickson, A. G., Wesolowski, D. J., Palmer, D. A., & Mesmer, R. E. (1990). Dissociation constant of bisulfate ion in aqueous sodium chloride solutions to 250.degree.C. *Journal of Physical Chemistry*, *94*(20), 7978–7985. https://doi.org/10.1021/j100383a042

Ducklow, H., Fraser, W., Meredith, M., Stammerjohn, S., Doney, S., Martinson, D., et al. (2013). West Antarctic Peninsula: An ice-dependent coastal marine ecosystem in transition. *Oceanography*, *26*(3), 190–203. https://doi.org/10.5670/oceanog.2013.62

Ducklow, H. W., Stukel, M. R., Eveleth, R., Doney, S. C., Jickells, T., Schofield, O., et al. (2018). Spring-summer net community production, new production, particle export and related water column biogeochemical processes in the marginal sea ice zone of the Western Antarctic Peninsula 2012–2014. *Philosophical Transactions of the Royal Society A: Mathematical, Physical and Engineering Sciences*, *376*(2122). https://doi.org/10.1098/rsta.2017.0177

Emerson, S., & Hedges, J. (2008). *Chemical oceanography and the marine carbon cycle*. Cambridge University Press. https://doi.org/10.1017/CBO9780511793202

Evans, W., Mathis, J. T., Cross, J. N., Bates, N. R., Frey, K. E., Else, B. G. T., et al. (2015). Sea-air CO_2 exchange in the western Arctic coastal ocean. *Global Biogeochemical Cycles*, *29*(8), 1190–1209. https://doi.org/10.1002/2015gb005153

Eveleth, R., Cassar, N., Sherrell, R. M., Ducklow, H., Meredith, M. P., Venables, H. J., et al. (2017). Ice melt influence on summertime net community production along the Western Antarctic Peninsula. *Deep Sea Research Part II: Topical Studies in Oceanography*, *139*, 89–102. https://doi.org/10.1016/j.dsr2.2016.07.016

Fassbender, A. J., Sabine, C. L., & Cronin, M. F. (2016). Net community production and calcification from 7 years of NOAA Station Papa Mooring measurements. *Global Biogeochemical Cycles*, *30*(2), 250–267. https://doi.org/10.1002/2015gb005205

Garibotti, I., Vernet, M., Ferrario, M., Smith, R., Ross, R., & Quetin, L. (2003). Phytoplankton spatial distribution patterns along the Western Antarctic Peninsula (Southern Ocean). *Marine Ecology Progress Series*, *261*, 21–39. https://doi.org/10.3354/meps261021

Gray, A. R., Johnson, K. S., Bushinsky, S. M., Riser, S. C., Russell, J. L., Talley, L. D., et al. (2018). Autonomous biogeochemical floats detect significant carbon dioxide outgassing in the high-latitude Southern Ocean. *Geophysical Research Letters*, *45*(17), 9049–9057. https://doi.org/10.1029/2018gl078013

Hauri, C., Doney, S. C., Takahashi, T., Erickson, M., Jiang, G., & Ducklow, H. W. (2015). Two decades of inorganic carbon dynamics along the West Antarctic Peninsula. *Biogeosciences*, *12*(22), 6761–6779. https://doi.org/10.5194/bg-12-6761-2015

Hoppema, M., Middag, R., De Baar, H. J. W., Fahrbach, E., Van Weerlee, E. M., & Thomas, H. (2007). Whole season net community production in the Weddell Sea. *Polar Biology*, *31*(1), 101–111. https://doi.org/10.1007/s00300-007-0336-5

Huang, K., Ducklow, H., Vernet, M., Cassar, N., & Bender, M. L. (2012). Export production and its regulating factors in the West Antarctica Peninsula region of the Southern Ocean. *Global Biogeochemical Cycles*, *26*(2). https://doi.org/10.1029/2010gb004028

Joy-Warren, H. L., van Dijken, G. L., Alderkamp, A. C., Leventer, A., Lewis, K. M., Selz, V., et al. (2019). Light is the primary driver of early season phytoplankton production along the western Antarctic Peninsula. *Journal of Geophysical Research: Oceans*, *124*(11), 7375–7399. https://doi.org/10.1029/2019JC015295

Kim, H., Doney, S. C., Iannuzzi, R. A., Meredith, M. P., Martinson, D. G., & Ducklow, H. W. (2016). Climate forcing for dynamics of dissolved inorganic nutrients at Palmer Station, Antarctica: An interdecadal (1993–2013) analysis. *Journal of Geophysical Research: Biogeosciences*, *121*(9), 2369–2389. https://doi.org/10.1002/2015jg003311

Kim, H., & Ducklow, H. W. (2016). A decadal (2002–2014) analysis for dynamics of heterotrophic bacteria in an Antarctic coastal ecosystem: Variability and physical and biogeochemical forcings. *Frontiers in Marine Science*, *3*(214). https://doi.org/10.3389/fmars.2016.00214

Kim, H., Ducklow, H. W., Abele, D., Barlett, E. M. R., Buma, A. G. J., Meredith, M. P., et al. (2018). Inter-decadal variability of phytoplankton biomass along the coastal West Antarctic Peninsula. *Philosophical Transactions of the Royal Society A: Mathematical, Physical and Engineering Sciences*, *376*(2122). https://doi.org/10.1098/rsta.2018.0170

Lee, K., Kim, T.-W., Byrne, R. H., Millero, F. J., Feely, R. A., & Liu, Y.-M. (2010). The universal ratio of boron to chlorinity for the North Pacific and North Atlantic oceans. *Geochimica et Cosmochimica Acta*, *74*(6), 1801–1811. https://doi.org/10.1016/j.gca.2009.12.027

Legge, O. J., Bakker, D. C. E., Johnson, M. T., Meredith, M. P., Venables, H. J., Brown, P. J., & Lee, G. A. (2015). The seasonal cycle of ocean-atmosphere CO_2 flux in Ryder Bay, West Antarctic Peninsula. *Geophysical Research Letters*, *42*(8), 2934–2942. https://doi.org/10.1002/2015gl063796

Legge, O. J., Bakker, D. C. E., Meredith, M. P., Venables, H. J., Brown, P. J., Jones, E. M., & Johnson, M. T. (2017). The seasonal cycle of carbonate system processes in Ryder Bay, West Antarctic Peninsula. *Deep Sea Research Part II: Topical Studies in Oceanography*, *139*, 167–180. https://doi.org/10.1016/j.dsr2.2016.11.006

Lueker, T. J., Dickson, A. G., & Keeling, C. D. (2000). Ocean $p\text{CO}_2$ calculated from dissolved inorganic carbon, alkalinity, and equations for K_1 and K_2: Validation based on laboratory measurements of CO_2 in gas and seawater at equilibrium. *Marine Chemistry*, *70*(1), 105–119. https://doi.org/10.1016/s0304-4203(00)00022-0

Marshall, G. J. (2003). Trends in the Southern Annular Mode from observations and reanalyses. *Journal of Climate*, *16*(24), 4134–4143. https://doi.org/10.1175/1520-0442(2003)016<4134:titsam>2.0.co;2

Martinson, D. G., & McKee, D. C. (2012). Transport of warm Upper Circumpolar Deep Water onto the Western Antarctic Peninsula continental shelf. *Ocean Science*, *8*(4), 433–442. https://doi.org/10.5194/os-8-433-2012

Martinson, D. G., Stammerjohn, S. E., Iannuzzi, R. A., Smith, R. C., & Vernet, M. (2008). Western Antarctic Peninsula physical oceanography and spatio-temporal variability. *Deep Sea Research Part II: Topical Studies in Oceanography*, *55*(18–19), 1964–1987. https://doi.org/10.1016/j.dsr2.2008.04.038

Meredith, M. P., & King, J. C. (2005). Rapid climate change in the ocean west of the Antarctic Peninsula during the second half of the 20th century. *Geophysical Research Letters*, *32*(19), 1–5. https://doi.org/10.1029/2005gl024042

Montes-Hugo, M., Doney, S. C., Ducklow, H. W., Fraser, W., Martinson, D., Stammerjohn, S. E., & Schofield, O. (2009). Recent changes in phytoplankton communities associated with rapid regional climate change along the western Antarctic Peninsula. *Science*, *323*(5920), 1470–1473. https://doi.org/10.1126/science.1164533

Montes-Hugo, M., Sweeney, C., Doney, S. C., Ducklow, H., Frouin, R., Martinson, D. G., et al. (2010). Seasonal forcing of summer dissolved inorganic carbon and chlorophyll a on the western shelf of the Antarctic Peninsula. *Journal of Geophysical Research*, *115*(C3). https://doi.org/10.1029/2009jc005267

Moreau, S., Mostajir, B., Bélanger, S., Schloss, I. R., Vancoppenolle, M., Demers, S., & Ferreyra, G. A. (2015). Climate change enhances primary production in the western Antarctic Peninsula. *Global Change Biology*, *21*(6), 2191–2205. https://doi.org/10.1111/gcb.12878

Roobaert, A., Laruelle, G. G., Landschützer, P., Gruber, N., Chou, L., & Regnier, P. (2019). The spatiotemporal dynamics of the sources and sinks of CO_2 in the global coastal ocean. *Global Biogeochemical Cycles*, *33*(12), 1693–1714. https://doi.org/10.1029/2019gb006239

Saenz, B. T., & Arrigo, K. R. (2014). Annual primary production in Antarctic sea ice during 2005–2006 from a sea ice state estimate. *Journal of Geophysical Research: Oceans*, *119*(6), 3645–3678. https://doi.org/10.1002/2013jc009677

Schofield, O., Brown, M., Kohut, J., Nardelli, S., Saba, G., Waite, N., & Ducklow, H. (2018). Changes in the upper ocean mixed layer and phytoplankton productivity along the West Antarctic Peninsula. *Philosophical Transactions of the Royal Society A: Mathematical, Physical and Engineering Sciences*, *376*(2122), 20170173. https://doi.org/10.1098/rsta.2017.0173

Schofield, O., Ducklow, H. W., Martinson, D. G., Meredith, M. P., Moline, M. A., & Fraser, W. R. (2010). How do polar marine ecosystems respond to rapid climate change? *Science*, *328*(5985), 1520–1523. https://doi.org/10.1126/science.1185779

Schultz, C. (2019). *A modeling study of the marine biogeochemistry, plankton dynamics, and carbon cycle on the continental shelf off the West Antarctic Peninsula*. Massachusetts Institute of Technology. Retrieved from https://doi.org/10.1575/1912/24019

Schultz, C., Doney, S. C., Zhang, W. G., Regan, H. C., Holland, P., Meredith, M., & Stammerjohn, S. (2020). Modeling of the influence of sea ice cycle and Langmuir circulation on the upper ocean mixed layer depth and freshwater distribution at the West Antarctic Peninsula. *Earth and Space Science Open Archive*. https://doi.org/10.1002/essoar.10502066.1

Shadwick, E. H., De Meo, O. A., Schroeter, S., Arroyo, M. C., Martinson, D. G., & Ducklow, H. W. (2021). Sea ice suppression of CO_2 outgassing in the West Antarctic Peninsula: Implications for the evolving Southern Ocean Carbon Sink. *Geophysical Research Letters*.

Smith, R. C., Baker, K. S., & Vernet, M. (1998). Seasonal and interannual variability of phytoplankton biomass west of the Antarctic Peninsula. *Journal of Marine Systems*, *17*(1–4), 229–243. https://doi.org/10.1016/s0924-7963(98)00040-2

Stammerjohn, S. E., Martinson, D. G., Smith, R. C., & Iannuzzi, R. A. (2008a). Sea ice in the Western Antarctic Peninsula region: Spatio-temporal variability from ecological and climate change perspectives. *Deep Sea Research Part II: Topical Studies in Oceanography*, *55*(18–19), 2041–2058. https://doi.org/10.1016/j.dsr2.2008.04.026

Stammerjohn, S. E., Martinson, D. G., Smith, R. C., Yuan, X., & Rind, D. (2008b). Trends in Antarctic annual sea ice retreat and advance and their relation to El Niño–Southern Oscillation and Southern Annular Mode variability. *Journal of Geophysical Research*, *113*(C3). https://doi.org/10.1029/2007jc004269

Stammerjohn, S., Massom, R., Rind, D., & Martinson, D. (2012). Regions of rapid sea ice change: An inter-hemispheric seasonal comparison. *Geophysical Research Letters*, *39*(6), 1–8. https://doi.org/10.1029/2012gl050874

Stukel, M. R., Asher, E., Couto, N., Schofield, O., Strebel, S., Tortell, P., & Ducklow, H. W. (2015). The imbalance of new and export production in the western Antarctic Peninsula, a potentially "leaky" ecosystem. *Global Biogeochemical Cycles*, *29*(9), 1400–1420. https://doi.org/10.1002/2015gb005211

Sweeney, C., Hansell, D. A., Carlson, C. A., Codispoti, L. A., Gordon, L. I., Marra, J., et al. (2000). Biogeochemical regimes, net community production and carbon export in the Ross Sea, Antarctica. *Deep Sea Research Part II: Topical Studies in Oceanography*, *47*(15–16), 3369–3394. https://doi.org/10.1016/s0967-0645(00)00072-2

Takahashi, T., Sutherland, S. C., Wanninkhof, R., Sweeney, C., Feely, R. A., Chipman, D. W., et al. (2009). Climatological mean and decadal change in surface ocean pCO_2, and net sea-air CO_2 flux over the global oceans. *Deep Sea Research Part II: Topical Studies in Oceanography*, *56*(8–10), 554–577. https://doi.org/10.1016/j.dsr2.2008.12.009

Tortell, P. D., Asher, E. C., Ducklow, H. W., Goldman, J. A. L., Dacey, J. W. H., Grzymski, J. J., et al. (2014). Metabolic balance of coastal Antarctic waters revealed by autonomous pCO_2 and $\Delta O_2/Ar$ measurements. *Geophysical Research Letters*, *41*(19), 6803–6810. https://doi.org/10.1002/2014gl061266

Turner, J., Barrand, N. E., Bracegirdle, T. J., Convey, P., Hodgson, D. A., Jarvis, M., et al. (2014). Antarctic climate change and the environment: An update. *Polar Record*, *50*(3), 237–259. https://doi.org/10.1017/s0032247413000296

Van Heuven, S., Pierrot, D., Rae, J. W. B., Lewis, E., & Wallace, D. W. R. (2011). *CO2SYS v 1.1, MATLAB program developed for CO$_2$ system calculations*. Oak Ridge, TN: ORNL/CDIAC-105b, Carbon Dioxide Information Analysis Center, Oak Ridge National Laboratory, U.S. DoE. Retrieved from https://doi.org/10.1017/CBO9781107415324.004

Wang, X., Yang, G.-P., López, D., Ferreyra, G., Lemarchand, K., & Xie, H. (2010). Late autumn to spring changes in the inorganic and organic carbon dissolved in the water column at Scholaert Channel, West Antarctica. *Antarctic Science*, *22*(2), 145–156. https://doi.org/10.1017/s0954102009990666

Wanninkhof, R. (2014). Relationship between wind speed and gas exchange over the ocean revisited. *Limnology and Oceanography: Methods*, *12*(6), 351–362. https://doi.org/10.4319/lom.2014.12.351

Williams, N. L., Juranek, L. W., Feely, R. A., Russell, J. L., Johnson, K. S., & Hales, B. (2018). Assessment of the carbonate chemistry seasonal cycles in the Southern Ocean from persistent observational platforms. *Journal of Geophysical Research: Oceans*, *123*(7), 4833–4852. https://doi.org/10.1029/2017jc012917

Yang, B., Emerson, S. R., & Bushinsky, S. M. (2017). Annual net community production in the subtropical Pacific Ocean from in situ oxygen measurements on profiling floats. *Global Biogeochemical Cycles*, *31*(4), 728–744. https://doi.org/10.1002/2016gb005545

Yang, B., Emerson, S. R., & Peña, M. A. (2018). The effect of the 2013–2016 high temperature anomaly in the subarctic Northeast Pacific (the "blob") on net community production. *Biogeosciences*, *15*(21), 6747–6759. https://doi.org/10.5194/bg-15-6747-2018